Selective fluorination of iodide-filled DWCNTs for stabilizing endohedral iron trifluoride

L. Doubtsof, C. Nie, Y. Ahmad, P. Bonnet, M. Monthioux, C. Taviot-Gueho, M. Dubois, Emmanuel Flahaut, K. Guérin

Selective Fluorination of iodide-filled DWCNTs for stabilizing endohedral iron trifluoride

L. DOUBTSOF[1], C. NIE[3], Y. AHMAD[2], P. BONNET[1], M. MONTHIOUX[4], C. TAVIOT-GUEHO[1], M. DUBOIS[1], E. FLAHAUT[3*], K. GUERIN[1*]

[1] *Université Clermont Auvergne, CNRS, Institut de Chimie de Clermont-Ferrand, 63000 Clermont-Ferrand, France*

[2] *Fahad Bin Sultan University, College of Science and Humanities, Department of Natural Sciences, Tabuk, 71454, Kingdom of Saudi Arabia*

[3] *CIRIMAT, Université Toulouse 3 Paul Sabatier, Toulouse INP, CNRS, Université de Toulouse, 118 Route de Narbonne, 31062 Toulouse cedex 9 - France*

[4] *CEMES, UPR-8011 CNRS, Université Toulouse 3 Paul Sabatier, France*

(*) katia.araujo_da_silva@uca.fr, emmanuel.flahaut@univ-tlse3.fr

KEYWORDS: DWCNTs, metatube, solid-gas fluorination, iron trifluoride, pair distribution function analysis, TEM

ABSTRACT

A novel approach to synthesizing iron trifluoride-filled carbon nanotubes by *in situ* selectively fluorinating an iron iodide precursor is presented. The potential of this method is explored, demonstrating the successful incorporation of iron trifluoride into the carbon nanotube structure. Various characterization techniques such as X-ray diffraction (XRD), PDF analysis managed at synchrotron, Raman spectroscopy, solid-state NMR, elemental analysis (EDS), and high-resolution transmission electron microscopy (HRTEM) were used to investigate the obtained hybrid nanomaterials. These characterization techniques provided a comprehensive understanding of the FeF_3@CNT hybrid nanomaterial, allowing for a thorough analysis of its structural and morphological properties. This knowledge is crucial for further optimizing the material's performance and tailoring it for specific applications in fields such as energy storage, catalysis, or medical uses.

GRAPHICAL ABSTRACT

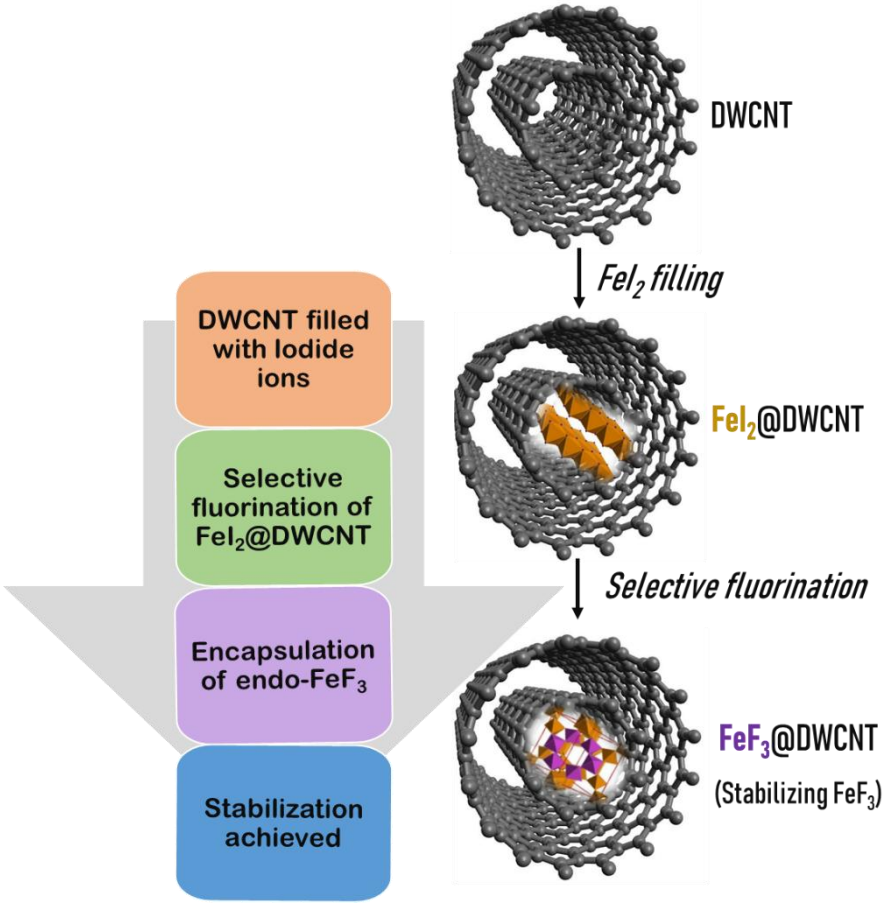

1. Introduction

Carbon nanotubes (CNTs) have garnered significant interest because of their amazing and one-of-a-kind properties [1]. These properties include high strength, excellent electrical conductivity, and thermal stability but more interestingly, combinations of such properties. Additionally, CNTs have a large specific surface area (SSA) [2-4] . These properties make CNTs highly suitable for a variety of applications. One promising technique is filling CNTs with inorganic compounds, which can prevent damaging (oxidation, hydration) and thus enhance properties like conductivity and electron transfer [5] , thus improving their efficacy in applications such as energy storage, drug delivery [6-8], sensors [9, 10] and catalysis [11]. Endochemistry applied to carbon nanotubes has indeed garnered significant attention from the scientific community [6-10].

Among inorganic materials, transition-metal fluorides, particularly iron trifluoride (FeF_3), have attracted significant scientific attention due to their unique electronic and magnetic properties. FeF_3 is a strong candidate for applications in catalysis, energy storage, and

magnetic materials [12-18]. However, FeF_3 faces challenges including low thermal stability and propensity to hydration. These issues can limit its performance, particularly in rechargeable batteries, where FeF_3 materials often experience rapid capacity loss and irreversible structural degradation. These limitations stem from the detachment of active iron species from the electrode surface and the formation of inactive phases, which reduce the material overall stability and efficiency [19-21]. In the field of catalysis, FeF_3 shows promise due to its potential to enhance chemical reactions, but its stability under certain reaction conditions remains inadequate. Additionally, the synthesis of FeF_3 often requires severe conditions, limiting its practical application. In medical applications, FeF_3 shows promise in drug delivery applications due to its favorable properties. The following are some relevant aspects to insure the possible uses of FeF3 in medical devices: i) Cell-derived nanovesicles are used for drug delivery in the central nervous system due to their stability, biocompatibility, and ability to penetrate biological barriers, including the blood-brain barrier [22]: their surfaces can be designed and adjusted to target the brain, ii) $FePO_4$ nanoparticles have been studied for drug delivery, with Fe^{3+}-DOX nanoparticles enhancing cytotoxicity by 10 times and stabilizing RNA and supporting mRNA translation activity [23], iii) surface-modified nanoparticles have been developed to enhance anti-tumor efficacy by improving cellular internalization, circulation time, and reducing toxicity [24], iv) biocompatible nanopolymers, with their high drug loading, controlled release, and biodegradation capabilities, can enhance biosensing applications and improve drug delivery systems [25]. In summary, FeF_3 and related nanomaterials have significant potential for targeted drug delivery, particularly in treating neurological diseases.

Various methods exist for filling CNTs with FeF_3, including chemical vapor deposition (CVD) and solution-based methods [26, 27]. A carbon source and FeF_3 precursor gases react in a high-temperature furnace to deposit FeF_3 inside nanotubes during CVD.

Solution-based methods dissolve FeF_3 in a solvent, and the nanotubes are immersed in the solution to achieve filling [28]. Both methods have specific advantages and can be tailored for different applications. Another approach utilizes capillary forces, relying on the surface tension of the molten compound (liquid FeF_3) to drive it into the nanotubes. This method is advantageous as it does not require complex equipment or any solvent and usually achieves good filling ratios [29-32].

In this work, we present a novel approach for filling double-walled carbon nanotubes (DWCNTs) with a molten iron-containing precursor (FeI_2) followed by in situ fluorination by

F_2 gaz to prepare FeF_3 directly within DWCNTs (FeF_3@CNT) and prevent the development of hydrated forms, which would decrease the material performance and stability.

2. Experimental part

2.1 Materials and syntheses

2.1.1 CNT pre-filling : synthesis of FeI_2@DWCNT

A previous study detailed the synthesis of DWCNTs [33] . The inner diameter distribution ranges from 0.5 to 2.5 nm in the sample. Approximately 80% of the sample consists of DWCNTs, with around 15% being SWCNTs and 5% triple-walled CNTs. A purification treatment combining heating in air at 550°C for 30 minutes followed by washing with concentrated HCl was applied as described in detail by Bortolamiol *et al* [34]. This purification treatment aimed to remove both residual catalytic metals (Co, Mo) and amorphous or low-cristallinity carbon material possibly containing heteroatoms, hereafter designated as disorganized carbon [35].

Dry purified DWCNTs were mixed with anhydrous FeI_2 [99.99% purity, Sigma Aldrich, 400858-1G], with a volumic ratio of *ca.* 30:1 (DWCNTs/FeI_2), and ground in a mortar to obtain a homogeneous mixture. The mixture was then transferred into a quartz ampoule (6 mm diameter) using a glass funnel. These steps were performed in a tent under a protective dry N_2 atmosphere because anhydrous FeI_2 is very hygroscopic. Subsequently, the ampoule was evacuated down to a reduced pressure of 20 Pa and subjected to this dynamic vacuum for 2 hours. Finally, the ampoule was sealed with a flame and placed into a furnace. The heating program was set as follows: from room temperature (RT) to 690°C at 5°C/min, with a 24-hour dwell at 690°C, then cooled down to 567°C at 0.1°C/min, then down to 467°C at 1°C/min, and finally down to RT at 5°C/min. Given the volumic ratio used, the filling material was in a large excess, requiring further washing to remove the excess of non-encapsulated material. To facilitate dissolution, an ultrasonication bath was used. The suspension was filtered and washed several times with a concentrated aqueous HCl solution (37%) to ensure the removal of excess filling material located outside the nanotubes. The washed solid was finally freeze-dried to prevent strong agglomeration upon drying.

2.1.2 Solid-gas fluorination

Given its high reactivity and specificity in introducing fluorine atoms into organic molecules [36], gaseous molecular fluorine (F_2) was selected as the fluorinating agent for this experiment. The use of gaseous molecular fluorine allows precise control over the fluorination process, ensuring high yields and minimal side reactions. Furthermore, the strong affinity between fluorine and iron facilitates the diffusion of fluorine into the nanotube cavity, promoting its migration into the nanotube structure. This process is crucial for achieving optimal catalytic activity, as hydrated forms can impede desired chemical reactions.

Solvay Fluor supplied the fluorine gas (purity 98-99% v/v, with HF max. 0.5% v/v and additional gases, notably O_2/N_2 at roughly 0.5% v/v). The experimental setup involved placing samples in a cylindrical nickel reactor which was previously passivated with NiF_2 to prevent corrosion (50 cm in length with a volume of approximately 1 liter). Selecting optimal fluorination conditions was paramount for enhancing the efficiency of the reaction. By precisely tuning experimental parameters such as temperature, pressure, and reactant concentrations, a significant level of fluorination was achieved while minimizing unwanted side reactions, especially the possible fluorination of DWCNTs themselves. Special emphasis should be given to selecting the optimal fluorination conditions to enhance the reaction efficiency [37-40]. Temperature control during the fluorination process is crucial to avoid damaging the nanotubes and ensure the full transformation of the contained FeI_2 into FeF_3. Additionally, monitoring the F/C atomic ratio is essential for maintaining the quality and integrity of the nanotubes i.e. limiting the fluorination of carbon only to the first wall [38, 40, 41] (Figure S1a).

Thermodynamic calculations were conducted at 50°C using FactWEB to determine the amount of fluorine required to convert FeI_2 to FeF_3 (Figure S1b). A molar ratio of F_2/FeI_2 higher than 6 resulted in the formation of gaseous species like IF_5 and IF_7, avoiding the presence of solid impurities in the sample, with FeF_3 being the sole solid species formed. Continuous injection of molecular fluorine into the furnace ensured a large excess of it, facilitating the fluorination process.

10 mg of FeI_2@DWCNT was introduced into the oven under a pure molecular F_2 flow at 50°C during 24 hours at 10 mL/min insuring a F_2/FeI_2 ratio higher than 6. 1 hour and 12 hours experiments weres also conducted to get some information on progressive transformation. However, when duration is not mentioned, the reference duration is 24h fluorination process. So, the total conversion of FeI_2 into FeF_3 was allowed owing to thermodynamic predictions.

Some graphite was also set in the cooled zone of the oven to catch the gaseous fluorides formed. Gradual diffusion of F_2 into the DWCNTs resulted in the exchange with iodine atoms. After fluorination, a mass loss of 22% was measured, in agreement with the disappearance of iodine in gaseous form, confirming the reactivity of FeI_2@DWCNT under F_2. For comparison purpose, DWCNT were fluorinated during 24h at 50°C and the obtained sample is DWCNT-F_2.

2.2 Physico-Chemical Characterization Techniques

2.2.1 High-Resolution Transmission Electron Microscopy (HRTEM)

All samples were imaged by HRTEM with a FEI Tecnai-F20 microscope (operated at 100 kV) with the objective lens equipped with a Cs corrector and a FEG-type electron source, and occasionally with a Philips CM30 microscope (operated at 150 kV) with a LaB_6 gun source. A JEOL JEM-ARM200F equipped with a STEM and Cs corrector for the condenser lens was used for ADF images and EELS analysis. To prepare the TEM specimen, samples were dispersed in ethanol using a sonication bath first. Then a few drops were deposited onto a copper grid (200 mesh) coated with a lacey-type carbon film, using a glass pipette. After the evaporation of the ethanol from the grid, the specimen was ready for TEM observation.

2.2.2 Pair distribution function PDF

Total X-ray scattering data were collected at the SOLEIL synchrotron on the X-ray powder diffraction station of the Cristal beamline in Debye–Scherrer mode. The wavelength of 0.436723 Å (28 keV) was selected using a double-crystal Si (111) monochromator and calibrated with a LaB_6 NIST standard. The diffractometer was equipped with a XPAD hybrid pixel detector, which is specifically designed to achieve an excellent signal-to-noise ratio and to handle time-resolved data sets. The powder samples were contained in glass capillaries with a diameter of 0.7 mm. Data collection was performed at room temperature over an angular range of 1-125° with a total acquisition time of 30 minutes

The two-dimensional raw data were converted to intensity versus 2Θ. The data were corrected and normalized using the program PDFgetX2 [42] and truncated at Q_max = 25 $Å^{-1}$ for FeI_2 and 17 $Å^{-1}$ for CNT-based samples and FeF_3, to obtain the optimized total scattering structure function S(Q) and the pair distribution function (PDF) G(r). Structural and quantitative phase analysis was carried out using the PDFgui software [43]. The ICSD database was used for

reference structures of FeI_2 (ICSD #52369), FeF_3 (ICSD #235864) and graphite (ICSD#76767).

2.2.3 Nuclear Magnetic Resonance (NMR)

NMR analysis was performed using a 300 MHz Bruker Advance spectrometer. NMR measurements were conducted on ^{19}F nuclei with Magic Angle Spinning (MAS) conditions. The measurements were carried out using a Bruker probe equipped with 2.5 mm rotors running at a spinning rate of 30 kHz. A simple $\pi/2$ pulse sequence was used with a $\pi/2$ pulse of 3 μs and recycling time of 3 s. Chemical shifts are referenced to $CFCl_3$.

2.2.4 Raman Spectroscopy

Raman spectra were recorded at a wavelength of 514.5 nm (corresponding to an energy of 2.41 eV) using a Jobin Yvon T64000 spectrometer working in confocal microscope mode. The power of the laser was tuned to 100 mW.

2.2.5 Thermogravimetric analysis

TGA measurements were conducted using a Mettler Toledo TGA/DSC1 instrument under both air and nitrogen atmospheres. The heating rate was set at 5°C per minute, and the temperature range spanned from 25 to 1100 °C.

3. Results and Discussion

The samples before and after the iodine-fluorine exchange, labeled as FeI_2@DWCNT and FeF_3@CNT respectively, were imaged with a transmission electron microscope (TEM). The TEM images are presented in Fig. 1. The FeI_2@DWCNT sample primarily consists of carbon nanotubes, organized into bundles, some exceeding 50 nm in width. The surface of the CNTs is coated with a compound identical to that found on purified CNTs, identified as disorganized carbon. Many tubes contain material within their inner cavities. Regions of high contrast, observed within the CNT bundles or isolated CNTs, exhibit a regular arrangement of black spots along the inner cavity of the CNT over a significant length, indicating the presence of FeI_2 (Fig. 1(a-d)). The one-dimensional morphology of the DWCNTs remains intact following fluorine treatment. The FeF_3@DWCNT sample primarily consists of CNTs, with no evidence of deterioration or deformation of the outer walls of the CNTs, which would reveal excessive fluorination. However, identifying the presence of FeF_3 in the cavities can be

challenging due to the lower contrast of fluorine compared to iodine. Therefore, it is necessary to employ an additional microscopic characterization method, such as dark-field microscopy, in this investigation.

Dark field microscopy utilizes an annular aperture located in the back focal plane of the objective lens to accentuate objects (or even single atoms, if allowed by the TEM resolution, which is the case here) that scatter electrons at wide angles. Typically, the heavier the atom, the higher the scattered intensity at wide angle. This aperture obscures transmitted beams while allowing diffracted beams at wide angles to pass through, resulting in brighter images of iron iodide and iron fluoride compared to carbon. Similarly, bright field microscopy employs a diaphragm in the focal plane of the lens to block diffracted beams at wide angles, enhancing image contrasts. Bright field microscopy highlights crystallized materials and/or materials with high molar mass, making them appear darker than disorganized and/or light atom materials. Examples of dark field and bright field images of the FeI_2@DWCNT sample are depicted in Fig. 2 and Fig. S2. In the bright field images, the FeI_2@DWCNT sample consists of bright nanowires of mean diameter 0.8 nm ranged between 0.2 and 2.8 nm (Fig. 3a). In the bright field image, these nanowires appear as dark lines or lines segments encapsulated within the CNTs. A statistical study of images using Imagej software by MET highlights an average atomic filling rate of 40% of nanotubes by FeI_2.

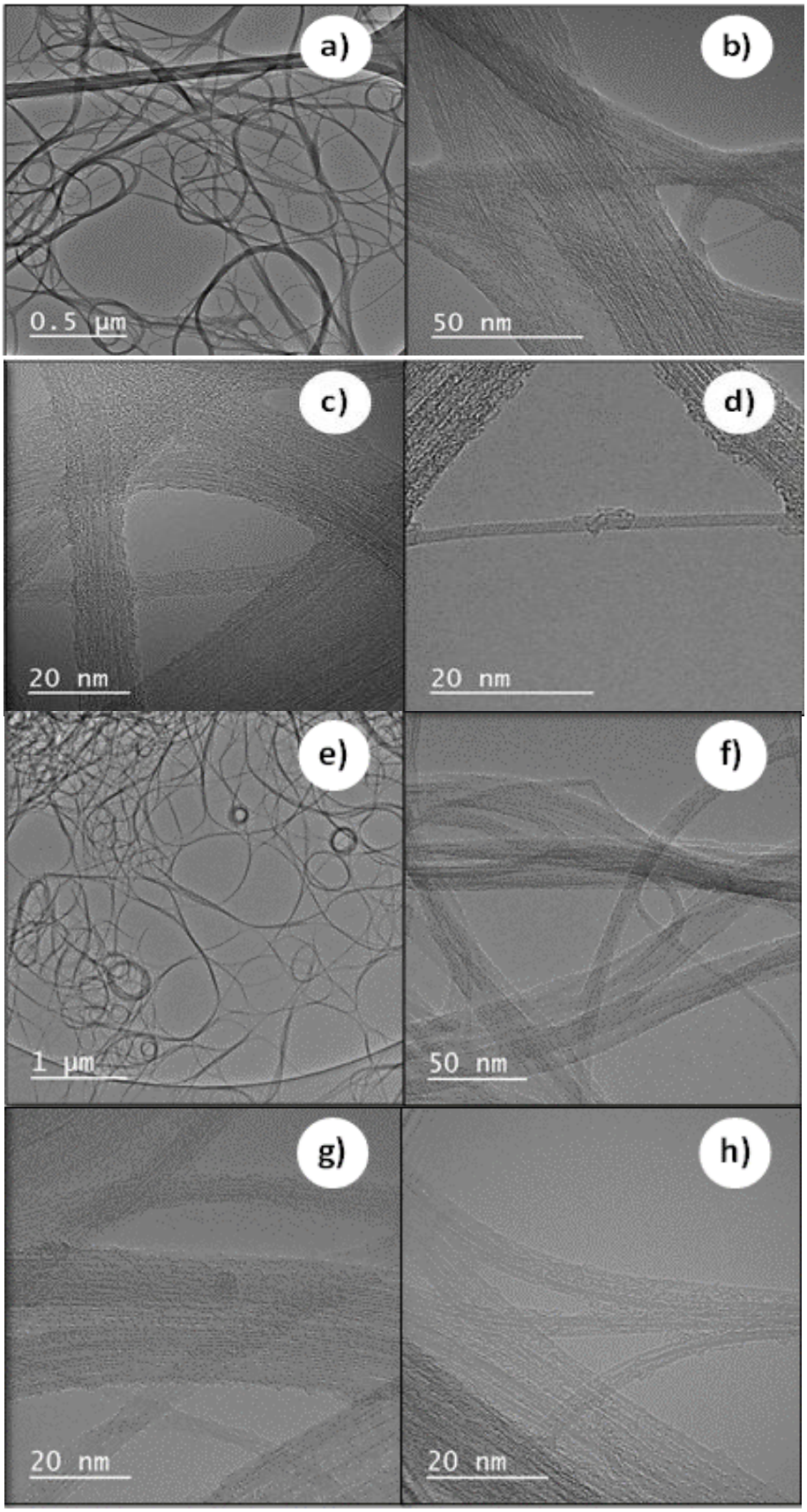

Fig. 1. High magnification TEM images of FeI_2@DWCNT sample (a-d) and FeF_3@DWCNT (e-h)

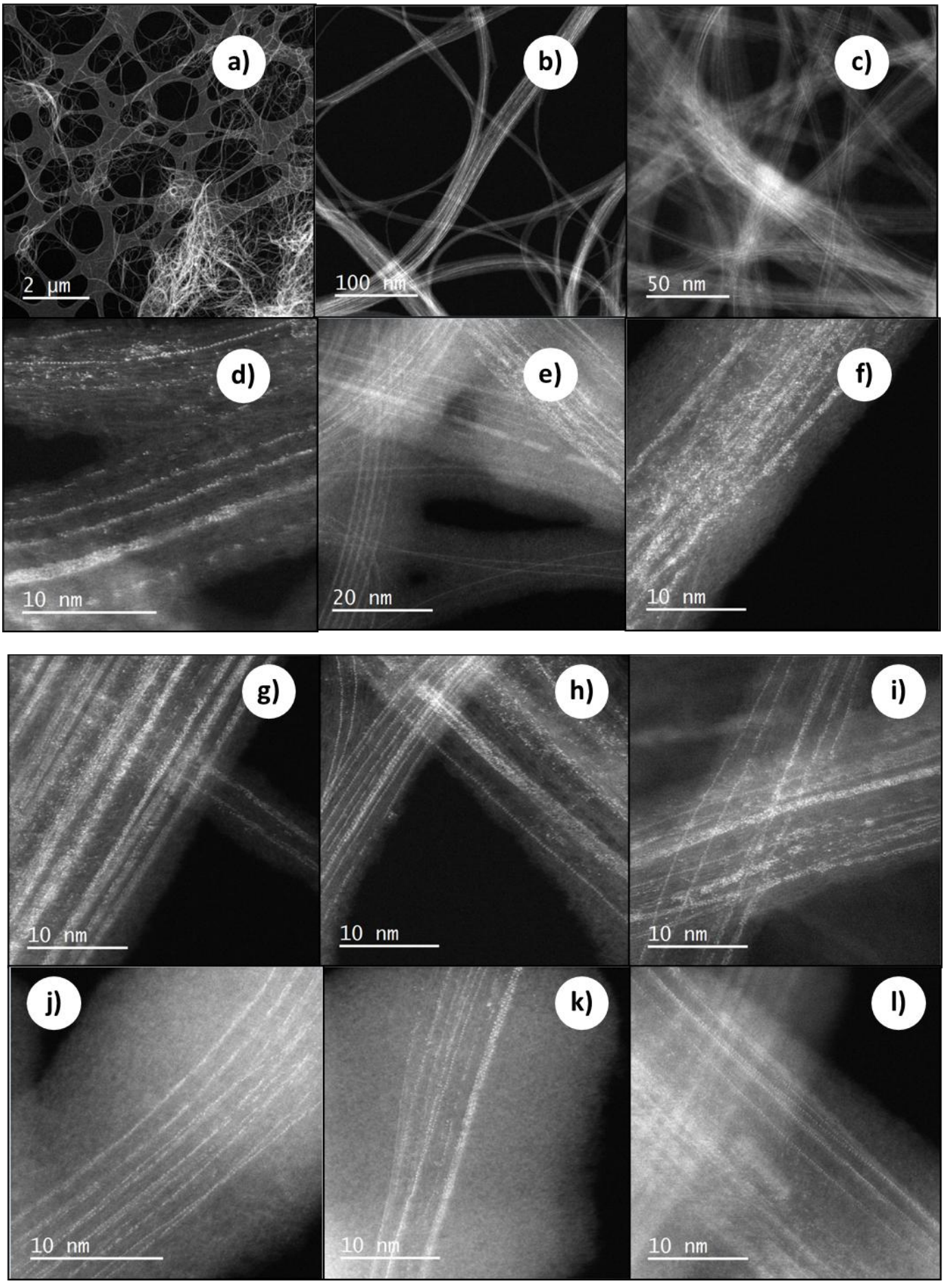

Fig. 2. High-angle annular dark-field images of FeF_3@DWCNT material

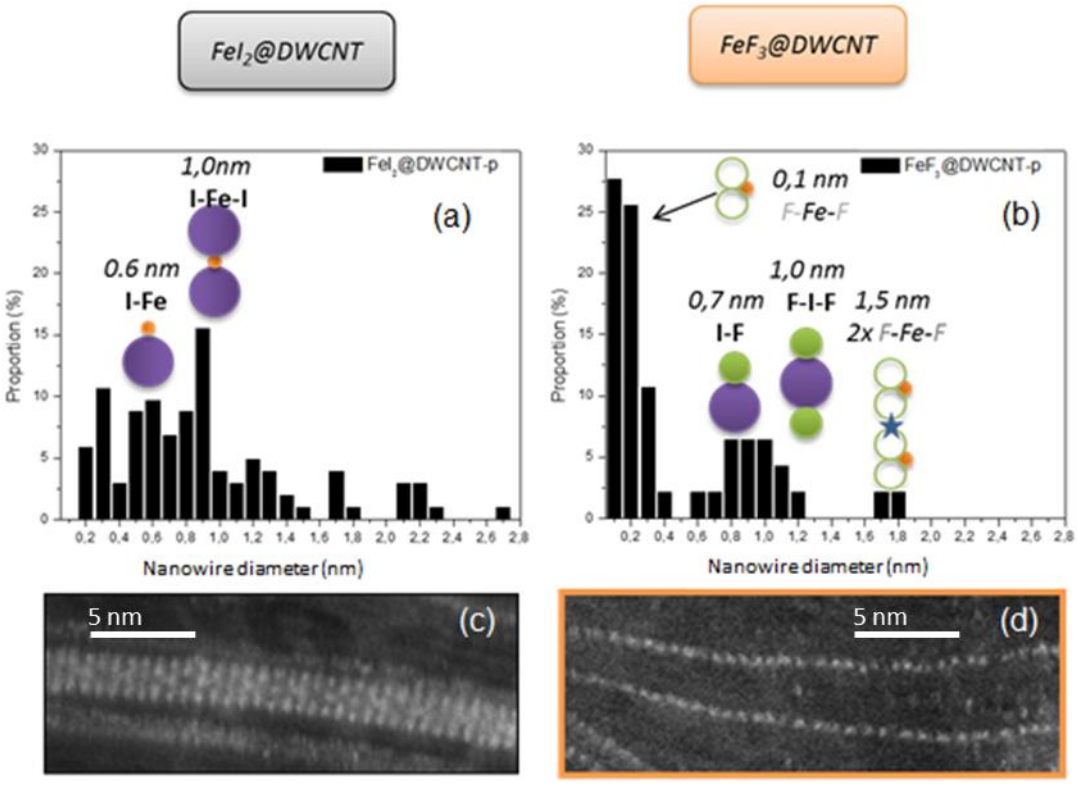

Fig. 3. Average diameter (a,b), obtained by analysis of dark-field images (c, d), of particle wires located in the inner tube of DWCNT before (a,c) and after fluorination (b,d).

The dark field images of the FeI_2@DWCNTs (Fig. 3c) reveal bright nanocrystals with a mean diameter of 0.8 nm, scattered within a range of 0.2 to 2.8 nm (Fig. 3a). In bright field images (Fig. S2), these nanowires are observed as dark linear areas surrounded by the CNTs. The filling material within isolated nanotubes in high-resolution dark-field images exhibits a well-organized pattern consisting of bright dots periodically displayed, revealing a crystallized structure. Fig. S3 displays dark field and bright field images of the FeF_3@DWCNT sample. In dark-field images, the DWCNTs contain bright nanowires or nanowire segments with diameters ranging from 0.1 nm to 1.8 nm (Fig. 3b). A reduction in nanowire diameter appears to be quite effective as a consequence of the fluorination. The bright zones consist of dots that align in a single direction, forming monoatomic chair sections (Fig. 3d). These variations observed before and after the iodine-fluoride exchange may be attributed to a modification in the crystalline structure within the tubes. Comparing the volume of the lattice in the FeI_2 structure to the number of atoms per unit, which is 96.03 / 1 = 96.03 $Å^3$, and then comparing it to the equivalent value of the FeF_3 structure, which is 311 / 6 = 51.83 $Å^3$, reveals that the nanowire diameter experiences an average contraction of approximately 50%.

EDX analysis of FeI_2@DWCNT confirms the simultaneous presence of iron and iodine elements in the starting material (Fig. S4). Additional peaks are observed in the spectrum, including copper (from the TEM grid), and cobalt (residue from the catalyst used in DWCNT synthesis) [44]. After fluorination, EDX spectroscopy reveals the presence of fluorine in the FeF_3@DWCNT sample, along with residual iodine, indicating incomplete I → F substitution (Fig. S5). It goes with the weight decrease registered after fluorination as only 22% weight loss has been registered. Through various microscopy techniques and associated methods, we can confidently confirm fluorination of the contained material without adverse effects on the tube walls of the initial sample. Additionally, we verify that iron fluorides are contained within the tubes and arranged in the form of nanowires.

To validate the hypothesized mechanism of FeF_3 generation together with release of IF_x molecule, a control experiment aiming at intercalating a graphite sample with IF_x molecules generated during the FeI_2 → FeF_3 transformation was made. It is commonly postulated that fluorinated iodine gases, specifically IF_x, which are generated during the process of fluorinating iron iodide, are effectively removed from the system by means of a gaseous fluoride flow attracted towards the cooler region of the oven. Lowering the temperature facilitates the occurrence of condensation and intercalation processes of fluorinated iodized species inside the interlayer regions. Therefore, it is feasible to ascertain the number of intercalated entities using mass measurement, and their characteristics can be identified by conducting structural characterizations. An aluminum vessel containing graphite, specifically sourced from the supplier TIMCAL with the designation KS15, is thereafter positioned within the refrigerated section of the oven.

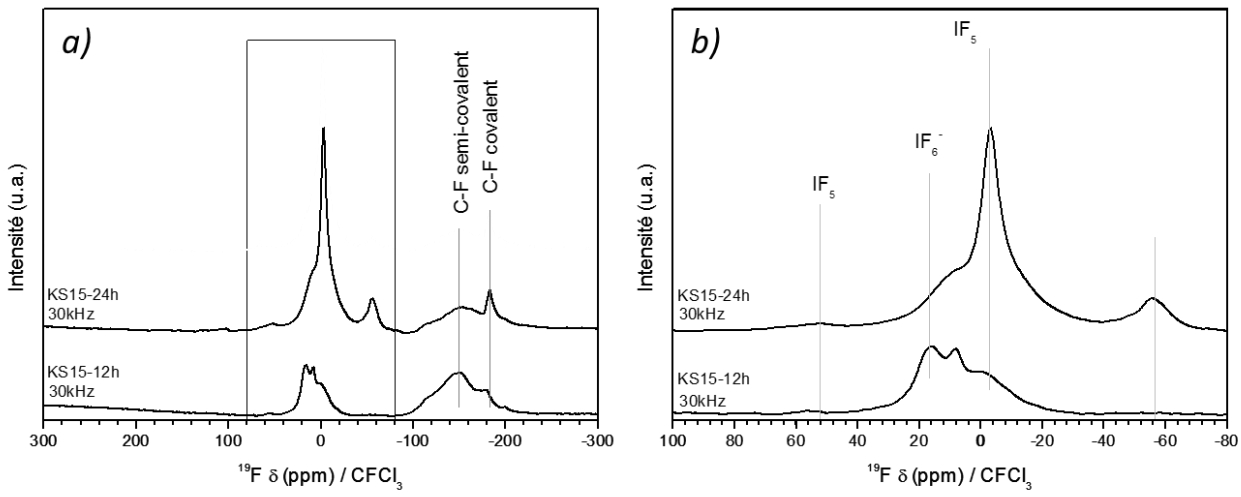

Fig. 4. a) ^{19}F NMR MAS spectra of graphite samples present in the cooler part of the oven during $FeI_2 \rightarrow FeF_3$ transformation for two durations (12 h and 24 h), b) zoom on iodine fluoride contributions

Within the specified range of 100 to -80 ppm, the ^{19}F MAS NMR spectra of the fluorinated graphite exhibit four narrow resonance bands, indicating the presence of fluoride species (Fig. 4). The narrowness is related to molecular motion within a confined structure. Species that are confined within the graphite interlayer spacing might be conceptualized as constituting a graphite intercalation complex. The observed bands at 8.2 and 56.4 ppm for the KS15-24h and KS15-12h samples, respectively, were assigned to IF_5 species, which align with the theoretical placements of 5 and 59 ppm [45]. The presence of a doublet with 1:4 ratio for the signal of IF_5 can be attributed to the structural arrangement of the molecule, which adopts a square-based pyramid geometry. This geometry results in the presence of two distinct fluorine positions inside the molecule, i.e. four F atoms in the square plan and one F perpendicular to this plane. In contrast, the spectra of the sample KS15-12h exhibits an additional band located at 16 ppm, which can be attributed to IF_6^- species [46]. Another band at -55.7 ppm suggests the presence of a species belonging to the IFx type with a maximum value of x equal to 4. The observation of this particular species is infrequent because to its inherent instability. It should be noted that the analysis of the KS15-1h sample was not possible due to the instability of the intercalated species that reacted as soon as the rotor was filled. As expected because of the fluorination at room temperature with a gaseous mixture of F_2 and IF_n species, a dual C-F bonding is obtained for both samples, resulting in two bands centered around -150 and -190 ppm which are assigned to semi-covalent and covalent C-F bonds. Those experiments clearly

evidence that gaseous iodide fluoride are released from the fluorination of FeI_2@DWCNT material.

X-ray diffraction was used to analyze the various materials under the high-energy flow of the SOLEIL synchrotron. To complement this analysis, pair distribution function (PDF) analysis was conducted on the diffraction patterns to obtain additional information.

The X-ray diffraction patterns of the samples, recorded at a wavelength of 0.436723 Å, are presented in Fig. 5. In comparison with bulk FeI_2 and FeF_3 materials, due to the complex morphology and limited structural coherence, the diffraction patterns of CNT-based materials exhibit a pronounced diffuse component and only a few Bragg peaks, namely the (002) peak corresponding to the periodic distance between graphene layers and the (100) and (110) peaks which relate to the hexagonal symmetry within a layer, referencing the well-known turbostratic graphenic structure.

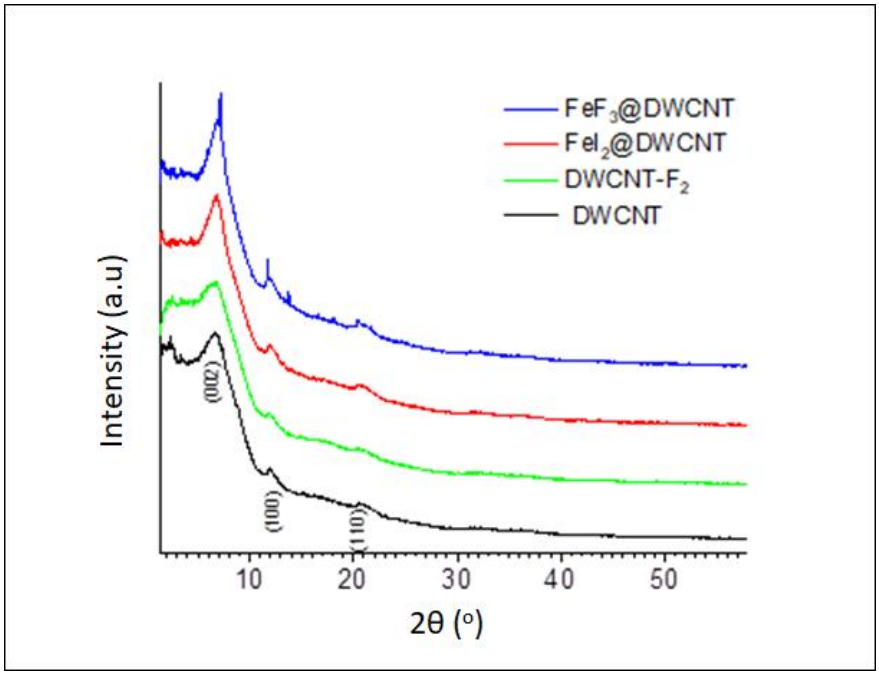

Fig. 5. X-ray diffraction patterns of DWCNT, DWCNT-F_2, FeI_2@DWCNT and FeF_3@ DWCNT

There are few differences between the diffraction patterns, except for a slight increase in the intensity of the 002 peak (improved signal-to-noise ratio) for the FeI_2@DWCNT and FeF_3@DWCNT compounds. This increase could be attributed to the presence of FeI_2 and FeF_3 within the nanotubes, respectively. Among the various crystallographic phases of FeF_3 (pyrochlore, Hexagonal Tungsten Bronze and rhombohedral), it will be the rhomboedral

phase that will be preferred latter in this paper thanks to annealing post-treatment. However, the position of this peak does not change, indicating that the structural integrity of the DWCNTs is not affected. Additionally, no visible modifications are observed in the in-plane direction, nor is there any indication of crystallized FeI_2 or FeF_3 as secondary phases. However, the dimensions of these encapsulated phases are quite small, in the range of few nm to below 1 nm, hence it is likely that the corresponding peaks are too broad to be visible. The main difference, in the case of FeF_3@DWCNT, is the presence of small, very fine peaks at the top of each broad peak; these indicate the presence of crystallized graphite-like carbon (ICSD#76767).

The iodine-fluorine exchange was checked on the FeI_2 control sample, whose diffraction data are presented in Fig. 6. After different fluorination times, a gradual disappearance of FeI_2 Bragg peaks and the presence of a disordered product were observed (Fig. 6a). The diffraction pattern of the sample obtained after 24 hours of fluorination does not show sharp diffraction peaks (Fig. 6a). The latter appear when the material is subjected to annealing at 600° C under nitrogen and corresponds to the rhombohedral phase of FeF_3 (ICSD #235864) (Fig. 6b).

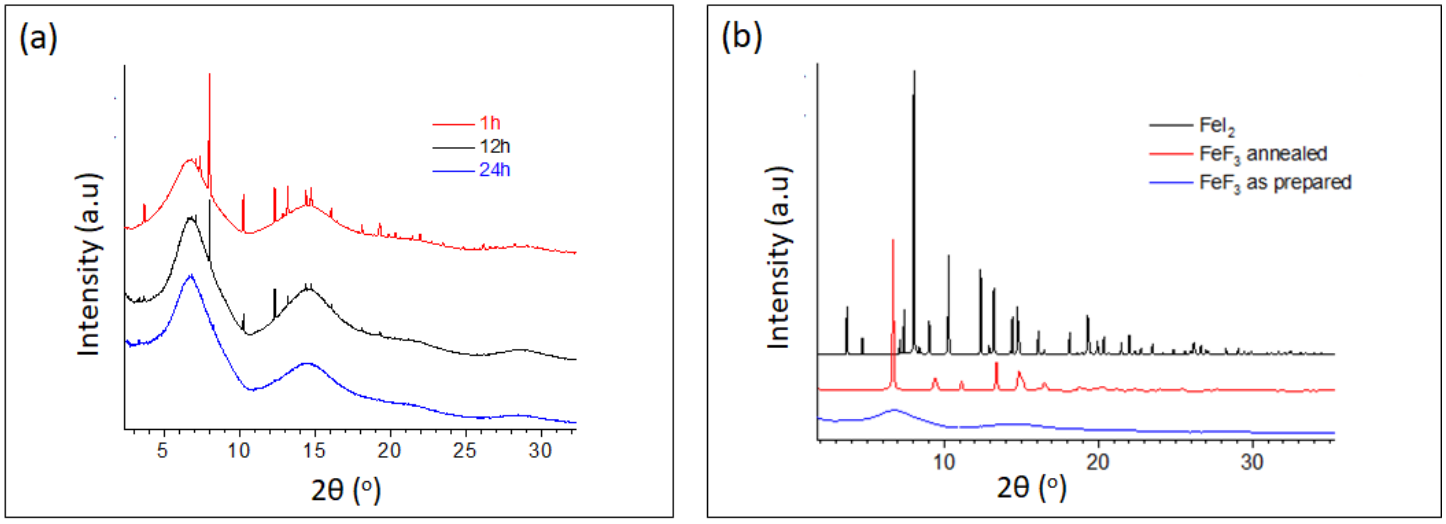

Fig. 6. X-ray diffraction patterns scattering data of a) FeI_2@DWCNT fluorinated under pure molecular fluorine during increasing durations and b) effect of annealing to detect the phase formed

To further interpret these X-ray scattering data, we extracted the pair distribution function (PDF), which provides an information on the atomic configuration of a compound through the distribution of interatomic distances, independent of its crystalline or amorphous state. In Fig. 7, the PDF functions of the FeI_2 control sample after different fluorination times are

presented. These clearly show the presence of nanometric domains (4-6 Å) with a well-defined internal structure. The first peaks at ~1.92 Å, 2.68 Å, and 3.71 Å are characteristic of Fe-F, F-F, and Fe-Fe distances in the rhombohedral FeF_3 structure. The amount of residual FeI_2 is very low, as the expected Fe-I, I-I, and Fe-Fe pairs at approximately 2.88 Å and 4.05 Å are not observed and must only contribute to the baseline width of the peaks. It should also be noted there is no significant increase of the size of the domains for FeF_3 with the duration of the fluorination.

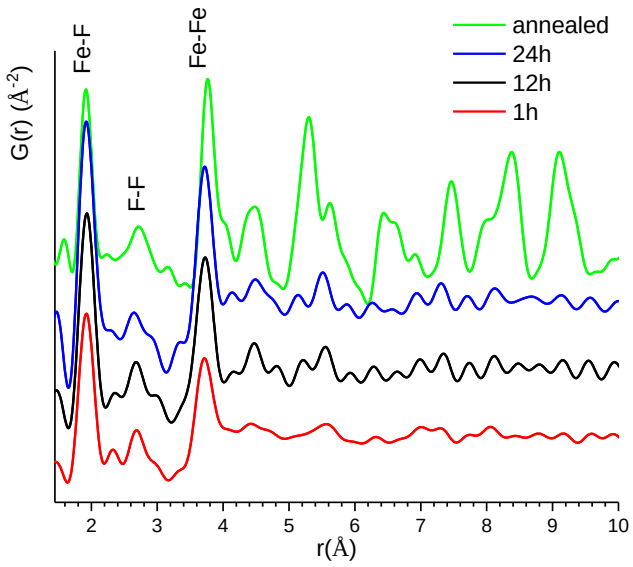

Fig. 7. PDF functions showing the transformation of FeI_2 to FeF_3 under fluorination at different times and after annealing

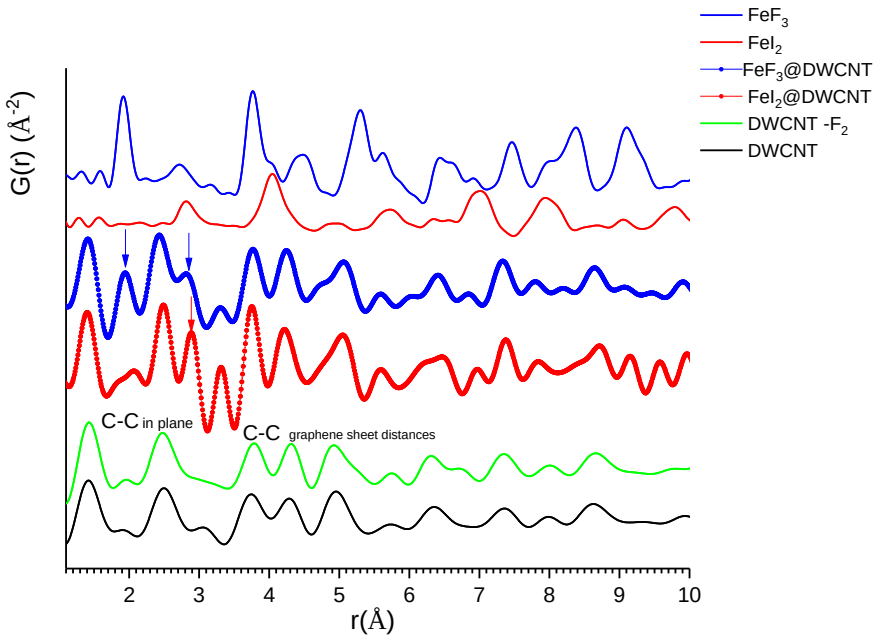

Fig. 8. Comparison in the range of distances up to 10 Å of the PDF functions of the DWCNT material alone before and after fluorination (identification of C-C distances), with those of the two filled-DWCNT materials (characteristic atomic pairs confirming the filling indicated by arrows), and those of crystallized FeI_2 and FeF_3

The PDFs of DWCNT samples are shown in Fig. 8 and Fig. S6. The first peaks are positioned at distances of 1.42 Å and 2.46 Å, which exactly match the in-plane C-C bond distances in the aromatic-type ring of graphite. No contribution of C-F bonds appears after fluorination confirming the absence of fluorination of DWCNTs at 50 C. From 3.4 Å, contributions of distances between graphene sheets (either within or between DWCNTs) are observed. The peaks are quite broad due to fluctuations of the intergraphene distances allowed by the turbostratic stacking (with respect to hexagonal stacking) and between DWCNTs within bundles to the next. The decay of the PDF beyond 10 Å indicates the loss of C-C coherences, probably due to the curvature of the graphene sheets.

Because of the broad character of the PDF peaks due to the small sizes ot the periodic volumes, it is difficult to examine C-C distance changes in the different samples. In fact, the peaks attributable to C-C distances overlap well in the range $1 < r < 10$ Å, indicating that the hexagonal symmetry of the graphene lattice is locally maintained. However, in the local r-range < 4 Å, there is an additional peak at 2.90 Å in the case of FeI_2@DWCNT and two

additional peaks at 1.95 Å and 2.84 Å in the case of FeF_3@DWCNT, which can be unambiguously attributed to the presence of FeI_2 and FeF_3, respectively. This could suggest that the domain size is limited to 3 Å due to the confinement of the materials within the nanotubes. However, it is important to keep in mind that other contributions may be present under the peaks attributed to C-C distances.

Raman spectroscopy (Fig. 9) stands as an unavoidable technique for probing charge transfer phenomena between carbon nanotubes (CNTs) and other materials. Typically, alterations in the Radial Breathing Modes (RBM) region and G bands serve as indicators of such transfers [47-52]. Notably, in the RBM modes and G bands, except for peaks in the range 190 – 230 cm^{-1}, no significant shifts are discerned, suggesting that charge transfer effects between CNTs and FeF_3 or FeI_2 are limited. Fig. 9 focues on the RBM modes, D, and G bands, with corresponding data detailed in Tables 1 and 2. Across all samples, RBM modes persist, with the absence of RBM mode extinction in FeI_2@DWCNT and FeF_3@DWCNT samples suggesting a notably low incidence of surface defects during various synthesis stages. The positioning of the outer tubes in DWCNTs remained consistent in all samples. However, a discernible frequency down-shift in the range 200-220 cm^{-1} is observed for the inner tubes of the FeI_2@DWCNT sample, indicating charge transfer between them and the encapsulated iron iodide, as reflected in Table 1. After the iodine-fluorine exchange, the RBM modes of the FeF_3@DWCNT sample realign with their original positions. However, one must have in mind that the filling could alter the resonance conditions, potentially making certain CNTs unobservable or bringing others into view. Some caution is needed when interpreting RBM shifts as a direct consequence of filling. A similar trend is observed in the G-band region (~1600 cm^{-1}), with a down-shift upon iron iodide filling, followed by restoration to the original position during iodine-fluorine exchange.

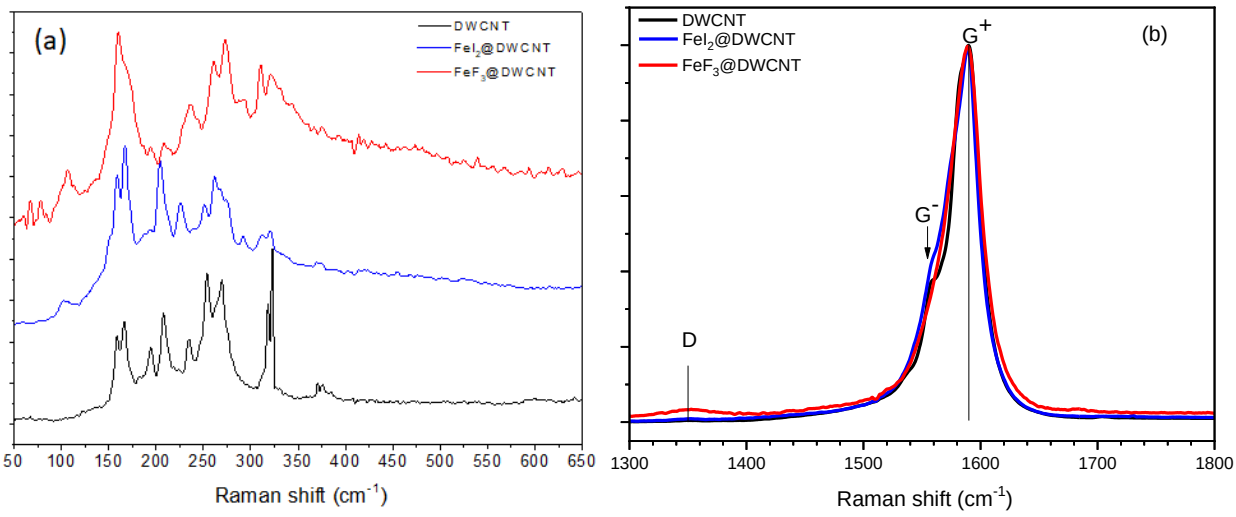

Fig. 9. (a) Raman spectra in the RBM modes area of DWCNT, FeI_2@CNT, and FeF_3@ DWCNT samples. (b) Raman spectra in the D-G bands region of the DWCNT, FeI_2@ DWCNT, and FeF_3@DWCNT samples

Table 1. Position of RBM (P) vibrations for purified DWCNT, FeI_2@DWCNT and FeF_3 @ DWCNT samples, along with the corresponding tube diameters (Ø) (P= C1/Ø +C2 where C1 and C2 are two recording condition-dependent constants taken to 223.5 and 12.5, respectively) and $\Delta Ø$ is the uncertainty in the tube diametre value

DWCNT			FeI_2@DWCNT			FeF_3@DWCNT		
P (cm^{-1}) ± 1	Ø (nm)	ΔØ (nm)	P (cm^{-1}) ± 1	Ø (nm)	ΔØ (nm)	P (cm^{-1}) ±1	Ø (nm)	ΔØ (nm)
159.1	1.52	0.01	159.1	1.52	0.01	160.4	1.51	0.009
166.2	1.45	0.009	167.5	1.44	0.009	167.5	1.44	0.009
194.5	1.23	0.006	193.3	1.24	0.006	194.5	1.23	0.006
208.1	1.14	0.005	204.2	1.17	0.006	208.1	1.14	0.005
234.5	1.01	0.004	225.5	1.05	0.005	236.5	0.998	0.004
253.9	0.926	0.004	251.3	0.936	0.004	261.0	0.899	0.003
269.4	0.870	0.003	262.3	0.895	0.003	273.3	0.857	0.003
/	/	/	292.6	0.798	0.003	293.9	0.794	0.003
318.4	0.731	0.002	312.0	0.746	0.002	310.7	0.750	0.002
322.3	0.721	0.002	319.7	0.728	0.002	322.3	0.721	0.002
370.7	0.624	0.002	369.4	0.626	0.002	/	/	/
375.8	0.615	0.002	373.2	0.620	0.002	375.2	0.616	0.002

Table 2. The positions of D and G bands, as well as the I_D/I_G ratio, measured for samples DWCNT (raw), FeI_2@DWCNT, and FeF_3@DWCNT.

Sample	D band	G^- band	G^+ band	I_D/I_G

	position (cm^{-1})	position (cm^{-1})	position (cm^{-1})	
DWCNT	1344 ± 1	1561 ± 1	1590 ± 1	0.02 ± 0.02
FeI_2@DWCNT		1565 ± 1	1591 ± 1	0 ± 0.02
FeF_3@DWCNT	1357 ± 1	1571 ± 1	1589 ± 1	0.02 ± 0.02

Fig. 10 depicts the thermal decomposition of selected samples including the references FeI_2, FeF_3 and DWCNTs in both air and N_2 environments. Notably, FeI_2@DWCNT exhibits a thermal behavior closely resembling to that of DWCNTs. Carbon emerges then as the predominant phase in this compound, as indicated. Under air exposure, FeI_2 undergoes atransformation into Fe_2O_3 at 200°C. When subjected to N_2, a significant weight loss occurs around 625°C, assigned to the solid-liquid transition and the equilibrium between vapor (lost in the gas stream) and liquid phases. Concerning DWCNT, primary weight loss is observed at 600°C in air (total combustion) and approximately at 900°C in nitrogen (-20%). Traces of oxygen in N_2 gas must be considered to explain such low thermal decompositon. Fig. 8(a) evidences significant differences for the thermal stabilities under air of FeI_2@DWCNT and bulk FeI_2. The conversion into Fe_2O_3 occurred in the ranges 110-290°C for the bulk and 200-470°C when FeI_2 is confined. Both the shift in temperature and the temperature spreading may be explained by the protection of the carbon lattice against oxidation; oxygen molecules must diffuse within the inner tubes for achieving the oxidation of the encapsulated material. The difference in the weight losses for FeI_2@DWCNT and DWCNT just before the beginning of the combustion of DWCNT, i.e. 7% at 450°C, is related to the presence of FeI_2 and may be used to estimate its relative content in the tubes, i.e. 10%w. The completion of the FeI_2 into Fe_2O_3 conversion is possibly not reached when the tubes start to decompose around 480°C. This estimation of 10% FeI_2 is then a minimum value. In inert gas, the TGA curves of FeI_2@DWCNT and DWCNT are also quite similar; the slight difference in the range 300-850°C is related to the lost of FeI_2 (vapor in equilibrium with the liquid phase).

The weight loss is continuous in air for the FeF_3 bulk from 300 to 880°C (Fig. 10b). The fluorination of FeI_2@DWCNT results in a decrease of the thermal stability. It is difficult to distinguish between 3 possible phenomena: i) conversion of residual FeI_2 into Fe_2O_3 ii) conversion of FeF_3 into Fe_2O_3 iii) oxidation of defected nanotubes resulting from the fluorination with F_2 and/or the reaction with IF_n gaseous species formed during the fluorination. In addition to the superimposition of those different mechanisms the higher weight losses in the 300-880°C range, for FeF_3@DWCNT compared to FeI_2@DWCNT may be also partly explained by residual IF_n species which are trapped into or onto the tubes. Because of these ambiguity about the thermal decomposition mechanisms, it is hazardous to

estimate the relative content of FeF_3, as we did for FeI_2. The completion of the oxidation in air is shifted by 100°C towards the low temperatures in relation with the defected nature of the sample after fluorination. The defects may favor the diffusion of oxygen towards the confined FeF_3 and FeI_2

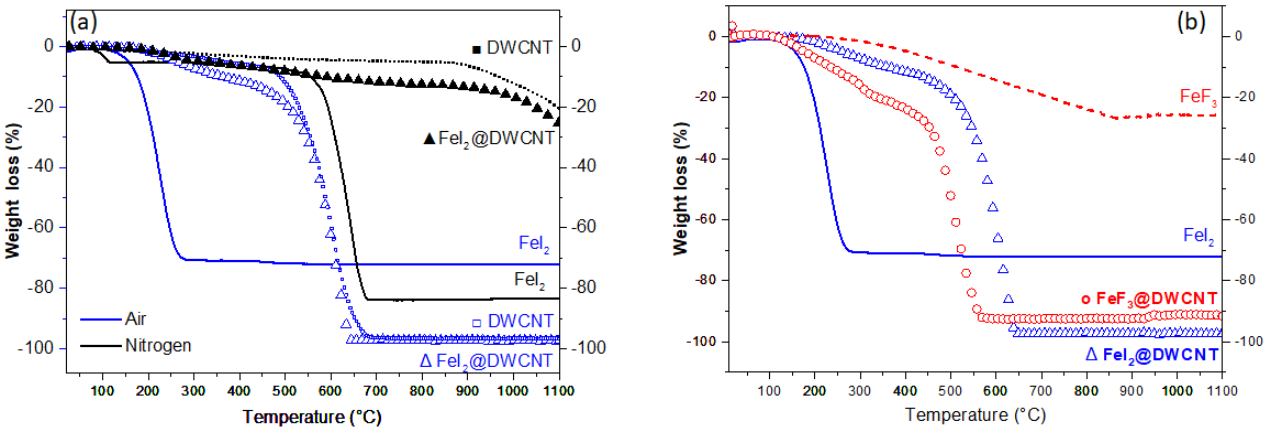

Fig. 10. Thermogramms obtained by TGA analysis under air or nitrogen of DWCNT, bulk FeI_2, FeI_2@ DWCNT (a) and only under air for FeF_3@DWCNT compared to FeI_2@ DWCNT as well as bulks FeF_3 and FeI_2 (b)

4. Conclusions

The study proposes a novel approach to synthesizing iron trifluoride-filled carbon nanotubes (FeF_3@CNT) via *in situ* selective fluorination of FeI_2 precursors (FeI_2@CNT). This methodological innovation offers significant promise for advancing the field of carbon nanotube endohedral functionalization by fluorides, expanding the repertoire of tailored hybrid nanomaterials. Through meticulous experimentation and comprehensive characterization, we demonstrate the successful incorporation of iron trifluoride into the carbon nanotube inner cavity, paving the way for a deeper understanding of the resulting nanocomposite properties and potential applications.

The results reveal the structural modifications induced by the fluorination process. Transmission electron microscopy images illustrate the preservation of the DWCNT structure following fluorination, with no evidence of drastic deterioration or deformation. Dark-field microscopy, coupled with elemental analysis using energy-dispersive X-ray spectroscopy, confirms the successful filling of DWCNTs with chain-like microstructure of iron trifluoride, elucidating the distribution and localization of the filling material within the nanotube cavities.

The confinement effect of FeI_2 in the tube is evidenced par themogravimetry analysis in air. The thermal stability in air is significantly changed after the fluorination of FeI_2@DWCNT. X-ray diffraction analysis, performed under synchrotron conditions reveals the distinct signal of FeF_3, indicating the successful transformation of FeI_2 to FeF_3 within the nanotube cavity. The conversion of FeI_2 to FeF_3 is accompanied by a loss of the crystalline nature of the iodide and a contraction in its volume. Pair distribution function (PDF) analysis further elucidates the structural characteristics through the interatomic distances, providing a comprehensive understanding of the nanocomposite's crystallographic features. Additionally, Raman spectroscopy reveals slight charge transfer phenomena and structural alterations induced by the incorporation of iron trifluoride.

Overall, the presented research represents a significant advancement in the field of carbon nanotube functionalization and hybrid nanomaterials. By leveraging selective fluorination techniques, the study demonstrates a viable strategy for enhancing the properties and functionalities of carbon nanotubes through the controlled incorporation of inorganic compounds. The comprehensive characterization and analysis conducted in this study lay the foundation for further optimization and tailoring of carbon nanotube-based materials for diverse applications in fields such as energy storage, catalysis, and biomedicine

Acknowledgements

The authors would like to thank Eric Elkaim for his support at the Cristal beamline. The authors also thank Soleil Synchrotron for supplying beamtime.

References

[1] A. Barzinjy, S. Hamad, M. Rashko, A. Hamad, Mechanical Properties of Carbon Nanotubes (CNTs): A Review, Eurasian J. Sci. Eng.8 (2022).
[2] A. Peigney, C. Laurent, E. Flahaut, R.R. Bacsa, A. Rousset, Specific surface area of carbon nanotubes and bundles of carbon nanotubes, Carbon 39(4) (2001) 507-514.
[3] B. Zhang, L. Zhang, Z. Wang, Q. Gao, An innovative wood derived carbon-carbon nanotubes-pyrolytic carbon composites with excellent electrical conductivity and thermal stability, J. Mater. Sci. Technol. 175 (2024) 22-28.
[4] P.G. Kumar, V. Kumaresan, R. Velraj, Stability, viscosity, thermal conductivity, and electrical conductivity enhancement of multi-walled carbon nanotube nanofluid using gum arabic, Fuller. Nanotub. Carbon Nanostructures 25(4) (2017) 230-240.
[5] G. Chimowa, M. Sendova, E. Flahaut, D. Churochkin, S. Bhattacharyya, Tuning the electrical transport properties of double-walled carbon nanotubes by semiconductor and semi-metal filling, J. Appl. Phys. 110(12) (2011).

[6] V. Neves, E. Heister, S. Costa, C. Tîlmaciu, E. Flahaut, B. Soula, H.M. Coley, J. McFadden, S.R. Silva, Design of double-walled carbon nanotubes for biomedical applications, Nanotechnology 23(36) (2012) 365102.
[7] E. Heister, C. Lamprecht, V. Neves, C. Tîlmaciu, L. Datas, E. Flahaut, B. Soula, P. Hinterdorfer, H.M. Coley, S.R.P. Silva, J. McFadden, Higher Dispersion Efficacy of Functionalized Carbon Nanotubes in Chemical and Biological Environments, ACS Nano 4(5) (2010) 2615-2626.
[8] V. Sanz, C. Tilmacîu, B. Soula, E. Flahaut, H.M. Coley, S.R.P. Silva, J. McFadden, Chloroquine-enhanced gene delivery mediated by carbon nanotubes, Carbon 49(15) (2011) 5348-5358.
[9] G. Chimowa, L. Yang, P. Lonchambon, T. Hungría, L. Datas, C. Vieu, E. Flahaut, Tailoring of DWNTs for formaldehyde sensing through encapuslation of selected materials, Phys. Status Solidi A. 216 (2019).
[10] G. Chimowa, E. Flahaut, V.R. Sodisetti, S. Bhattacharyya, Converting Ambipolar Double-Walled Nanotube Bundles to Unipolar Carbon Nanotube Field-Effect Transistor Devices by Inner Functionalization, Phys. Status Solidi A. 220(12) (2023) 2200669.
[11] Y. Tijjani, High temperature applications of carbon nanotubes (CNTs) [v]: thermal conductivity of CNTs reinforced silica nanocomposite, Bayero Journal of Pure and Applied Sciences (2022).
[12] J. Krishna Murthy, U. Gross, S. Rüdiger, E. Kemnitz, FeF3/MgF2: novel Lewis acidic catalyst systems, Appl. Catal. A-Gen. 278(1) (2004) 133-138.
[13] R.S. Rao, V. Pralong, U.V. Varadaraju, Facile synthesis and lithium reversible insertion on iron hydrated trifluorides FeF3·0.5H2O, Mater. Lett. 170 (2016) 130-134.
[14] F. Eveillard, Q. Loiseleux, R. Porhiel, M. El-Ghozzi, P. Bonnet, M.T. Sougrati, D. Delbegue, K. Guerin, Using innovative FeF3 cathode materials in Li batteries working under spacecraft applications, Solid State Ion. 387 (2022) 116079.
[15] T. Takami, K. Matsui, H. Senoh, N. Taguchi, M. Shikano, H. Sakaebe, T. Fukunaga, Magnetic behavior of Fe nanoparticles driven by phase transition of FeF3, J. Alloys Compd. 769 (2018) 539-544.
[16] Y. Wang, P. Zhou, M. Zhang, Z. He, Y. Cheng, Y. Zhou, F. Wu, High-performance honeycombed FeF3@C cathodes enabling practical lithium pouch cells and silicon−metal fluoride batteries, Energy Stor. Mater. 60 (2023) 102847.
[17] D.E. Conte, N. Pinna, A review on the application of iron(III) fluorides as positive electrodes for secondary cells, Mater. Renew. Sustain. Energy 3(4) (2014) 37.
[18] M. Kole, S. Khandekar, Engineering applications of ferrofluids: A review, J. Magn. Magn. Mater. 537 (2021) 168222.
[19] S. Matsuda, M. Ono, A. Myojin, Irreversible Structural Changes in Lithium Electrodes Accelerate Capacity Fading in Lithium-Metal-Based Rechargeable Batteries, ACS Appl. Energy Materials 6(4) (2023) 2524-2530.
[20] P. Chen, M. Ruck, A Stable Porous Aluminum Electrode with High Capacity for Rechargeable Lithium-Ion Batteries, Batteries 9(1) (2023) 37.
[21] S.-T. Myung, S. Sakurada, H. Yashiro, Y.-K. Sun, Iron trifluoride synthesized via evaporation method and its application to rechargeable lithium batteries, J. Power Sources 223 (2013) 1-8.
[22] Y. Liang, Z. Iqbal, J. Lu, J. Wang, H. Zhang, X. Chen, L. Duan, J. Xia, Cell-derived nanovesicle-mediated drug delivery to the brain: Principles and strategies for vesicle engineering, Mol. Ther.31(5) (2023) 1207-1224.
[23] S. Rayamajhi, S. Wilson, S. Aryal, R. DeLong, Biocompatible FePO4 Nanoparticles: Drug Delivery, RNA Stabilization, and Functional Activity, Nanoscale Res. Lett. 16(1) (2021) 169.

[24] A. Zeb, M. Gul, T.-T.-L. Nguyen, H.-J. Maeng, Recent progress and drug delivery applications of surface-functionalized inorganic nanoparticles in cancer therapy, J. Pharm. Investig. 53(6) (2023) 743-779.
[25] G. Ozcelikay, O. Esim, N.K. Bakirhan, A. Savaser, Y. Ozkan, S.A. Ozkan, Biocompatible Nanopolymers in Drug Delivery Systems and Their Recent Electrochemical Applications in Drug Assays, in: C.M. Hussain, S. Thomas (Eds.), Handbook of Polymer and Ceramic Nanotechnology, Springer International Publishing, Cham, 2021, pp. 875-894.
[26] S. Hampel, A. Leonhardt, D. Selbmann, K. Biedermann, D. Elefant, C. Müller, T. Gemming, B. Büchner, Growth and characterization of filled carbon nanotubes with ferromagnetic properties, Carbon 44(11) (2006) 2316-2322.
[27] C. Müller, D. Elefant, A. Leonhardt, B. Büchner, Incremental analysis of the magnetization behavior in iron-filled carbon nanotube arrays, J. Appl. Phys. 103(3) (2008).
[28] J. Jorge, E. Flahaut, F. Gonzalez-Jimenez, G. Gonzalez, J. Gonzalez, E. Belandria, J.M. Broto, B. Raquet, Preparation and characterization of α-Fe nanowires located inside double wall carbon nanotubes, Chem. Phys. Lett. 457(4) (2008) 347-351.
[29] J. Sloan, M.C. Novotny, S.R. Bailey, G. Brown, C. Xu, V.C. Williams, S. Friedrichs, E. Flahaut, R.L. Callender, A.P.E. York, K.S. Coleman, M.L.H. Green, R.E. Dunin-Borkowski, J.L. Hutchison, Two layer 4:4 co-ordinated KI crystals grown within single walled carbon nanotubes, Chem. Phys. Lett. 329(1) (2000) 61-65.
[30] G. Brown, S.R. Bailey, M. Novotny, R. Carter, E. Flahaut, K.S. Coleman, J.L. Hutchison, M.L.H. Green, J. Sloan, High yield incorporation and washing properties of halides incorporated into single walled carbon nanotubes, Appl. Phys. A 76(4) (2003) 457-462.
[31] E. Flahaut, J. Sloan, S. Friedrichs, A.I. Kirkland, K.S. Coleman, V.C. Williams, N. Hanson, J.L. Hutchison, M.L.H. Green, Crystallization of 2H and 4H PbI2 in Carbon Nanotubes of Varying Diameters and Morphologies, Chem. Mater. 18(8) (2006) 2059-2069.
[32] C. Nie, A.-M. Galibert, B. Soula, E. Flahaut, J. Sloan, M. Monthioux, A new insight on the mechanisms of filling closed carbon nanotubes with molten metal iodides, Carbon 110 (2016) 48-50.
[33] E. Flahaut, R. Bacsa, A. Peigney, C. Laurent, Gram-scale CCVD synthesis of double-walled carbon nanotubes, Chem. Commun. (12) (2003) 1442-1443.
[34] T. Bortolamiol, P. Lukanov, A.-M. Galibert, B. Soula, P. Lonchambon, L. Datas, E. Flahaut, Double-walled carbon nanotubes: Quantitative purification assessment, balance between purification and degradation and solution filling as an evidence of opening, Carbon 78 (2014) 79-90.
[35] K. Behler, S. Osswald, H. Ye, S. Dimovski, Y. Gogotsi, Effect of Thermal Treatment on the Structure of Multi-walled Carbon Nanotubes, J. Nanopart. Res. 8(5) (2006) 615-625.
[36] G.G. Furin, Use of Hydrogen Fluoride and Its Complexes with Bases for Introduction of Fluorine Atoms into Organic Molecules, ChemInform 34(27) (2003).
[37] Y. Ahmad, N. Batisse, M. Dubois, K. Guérin, F. Labbé, R. Metkemeijer, S. Berthon-Fabry, B. Molina Concha, F. Maillard, L. Dubau, R. Chattot, M. Chatenet, Fluorination of carbon based electrocatalysts for enhanced durability of PEMFC, SFEC Colloque de la Société Francophone d'Etude des Carbones, Carqueiranne, France, 2016.
[38] Y. Ahmad, E. Disa, K. Guérin, M. Dubois, E. Petit, A. Hamwi, P. Thomas, J.L. Mansot, Structure control at the nanoscale in fluorinated graphitized carbon blacks through the fluorination route, J. Fluor. Chem. 168 (2014) 163-172.
[39] Y. Ahmad, M. Dubois, K. Guerin, A. Hamwi, E. Flahaut, High energy density of primary lithium batteries working with sub-fluorinated few walled carbon nanotubes cathode, J. Alloys Compd. 726 (2017) 852-859.
[40] M. Chatenet, S. Berthon-Fabry, Y. Ahmad, K. Guérin, M. Colin, H. Farhat, L. Frezet, G. Zhang, M. Dubois, Fluorination and its Effects on Electrocatalysts for Low-Temperature Fuel Cells, Adv. Energy Mater. 13(15) (2023) 2204304.

[41] M. Dubois, N. Batisse, K. Guérin, P. Thomas, Fluorine: Characteristics, Chemistry and Applications Controlled fluorination using atomic fluorine, 2018.
[42] X. Qiu, J.W. Thompson, S.J.L. Billinge, PDFgetX2: a GUI-driven program to obtain the pair distribution function from X-ray powder diffraction data, J. Appl. Crystallogr. 37(4) (2004) 678-678.
[43] C.L. Farrow, P. Juhas, J.W. Liu, D. Bryndin, E.S. Božin, J. Bloch, T. Proffen, S.J.L. Billinge, PDFfit2 and PDFgui: computer programs for studying nanostructure in crystals, J. Phys. Condens. Matter 19(33) (2007) 335219.
[44] V. Datsyuk, C. Guerret-Piecourt, S. Dagreou, L. Billon, J.-C. Dupin, E. Flahaut, A. Peigney, C. Laurent, Double Walled Carbon Nanotube/Polymer Composites via in-situ Nitroxide Mediated Polymerisation of Amphiphilic Block Copolymers, Carbon 43 (2005) 873-876.
[45] M. Dubois, K. Guérin, J.P. Pinheiro, Z. Fawal, F. Masin, A. Hamwi, NMR and EPR studies of room temperature highly fluorinated graphite heat-treated under fluorine atmosphere, Carbon 42(10) (2004) 1931-1940.
[46] K. Guérin, J.P. Pinheiro, M. Dubois, Z. Fawal, F. Masin, R. Yazami, A. Hamwi, Synthesis and characterization of highly fluorinated graphite containing sp2 and sp3 carbon, Chem. Mater. 16(9) (2004) 1786-1792.
[47] J. Cambedouzou, J.L. Sauvajol, A. Rahmani, E. Flahaut, A. Peigney, C. Laurent, Raman spectroscopy of iodine-doped double-walled carbon nanotubes, Phys. Rev. B. 69(23) (2004) 235422.
[48] M. Sendova, E. Flahaut, B. DeBono, Raman spectroscopy of PbI2-filled double-walled carbon nanotubes, J. Appl. Phys. 98(10) (2005).
[49] J. González, C. Power, E. Belandria, J.M. Broto, P. Puech, J. Sloan, E. Flahaut, Pressure dependence of Raman modes in DWCNT filled with PbI2 semiconductor, physica status solidi (b) 244(1) (2007) 136-141.
[50] P. Puech, A. Ghandour, A. Sapelkin, C. Tinguely, E. Flahaut, D.J. Dunstan, W. Bacsa, Raman G band in double-wall carbon nanotubes combining p doping and high pressure, Phys. Rev. B. 78(4) (2008) 045413.
[51] E. Belandria, M. Millot, J.-M. Broto, E. Flahaut, F. Rodriguez, R. Valiente, J. Gonzalez, Pressure dependence of Raman modes in double wall carbon nanotubes filled with 1D Tellurium, Carbon 48(9) (2010) 2566-2572.
[52] M. Sendova, E. Flahaut, T. Hartsfield, Temperature dependence of Raman scattering in filled double-walled carbon nanotubes, J. Appl. Phys. 108(4) (2010).